

Adaptive Affinity Field for Semantic Segmentation

Tsung-Wei Ke*, Jyh-Jing Hwang*, Ziwei Liu, and Stella X. Yu

UC Berkeley / ICSI

Abstract. Existing semantic segmentation methods mostly rely on per-pixel supervision, unable to capture structural regularity present in natural images. Instead of learning to enforce semantic labels on individual pixels, we propose to enforce affinity field patterns in individual pixel neighbourhoods, i.e., the semantic label patterns of whether neighbouring pixels are in the same segment should match between the prediction and the ground-truth. The affinity fields characterize geometric relationships within the image, such as “motorcycles have round wheels”. We further develop a novel method for learning the optimal neighbourhood size for each semantic category, with an adversarial loss that optimizes over worst-case scenarios. Unlike the common Conditional Random Field (CRF) approaches, our adaptive affinity field (AAF) method has no extra parameters during inference, and is less sensitive to appearance changes in the image. Extensive evaluations on Cityscapes, PASCAL VOC 2012 and GTA5 datasets demonstrate the effectiveness and robustness of AAF in semantic segmentation.

Keywords: semantic segmentation; affinity field; adversarial learning

1 Introduction

Semantic segmentation is an important yet challenging task in computer vision, which requires assigning each pixel a categorical label, e.g., “motorcycle” or “person”. Recent advances in this field are mostly attributed to increasingly powerful pixel-wise classifiers (*unary predictions*) such as VGG-16 [1,2] and ResNet [3,4]. While the performance measured pixel-wise by e.g. mIoU is improving, there are often artifacts that appear totally avoidable to a layman observer. For example, wheels in “motorcycles” are circles with rods as support by design; but predicted label maps can not infer the structure of wheels, as demonstrated in Fig. 1 (c). In spite of big data, deep learning at per-pixel level seems unable to capture simple geometric regularities such as lines, contours, or more general micro-structures.

Various attempts have been made to incorporate structural reasoning into semantic segmentation, including Conditional Random Field (CRF) [5,6] and GAN [7,8]: **1**) CRF enforces label consistency between pixels, based on the input image appearance (e.g. RGB values) similarity. Global agreement can be achieved with message passing algorithms [9,10]. CRF is commonly employed as a post-processing step [5,11], or as a plug-in module inside deep neural networks [6,12]. Effective as it is, CRF is usually

* indicates equal contributions. Jyh-Jing is with the University of Pennsylvania. This work was done when he was a visiting researcher in Berkeley.



Fig. 1. Left to right: image, ground truth, softmax, affinity fields, and adaptive affinity fields. The inner structures in wheels are more prominent with affinity fields.

sensitive to input appearance changes and needs expensive iterative inference. **2)** GAN emerges as an alternative to enforce structural regularity in the data. Specifically, the predicted label map passes through a network which discriminates whether it looks like coming from the set of ground truth label maps. Promising as it is, GAN is observed to suffer from some usual problems such as unstable training and mode collapse [13].

We present a simple yet effective approach called **adaptive affinity fields (AAF)**. Unlike CRF and GAN that attempt to model the structural regularity based on the input/prediction appearance, our approach operates on the local affinity fields of prediction as well as ground-truth, requiring them to match in the properties derived from all the neighbourhoods instead of individual pixels.

Our main insight is as follows: Deep learning prizes itself on end-to-end learning, that is, if data (x_i, y_i) are the i -th sample observations from some underlying input-output mapping function g , i.e., $y = g(x)$, we devise a neural net $f(x; \theta)$ as a function approximator to g , and we learn it by minimizing the loss over $f(x_i)$ and measurement y_i . Our idea is that, we not only ask f to match g on x_i , but also ask $\mathcal{T}(f)$ to match $\mathcal{T}(g)$ at x_i , where \mathcal{T} is a projector that acts upon a function in the neighbourhood of x and $\mathcal{T}(f(x))$ maps the f values in x 's neighbourhood to a single value/vector at x . For example, if \mathcal{T} is a 5×5 average kernel, then we ask the average predictions in 5×5 windows to match those from the ground-truths.

As shown in Fig. 1 (d) and (e), local *affinity fields* characterize the second-order derived property of a given scene, usually corresponding to its intrinsic geometric structures. For instance, in streetview scenes, local affinity fields mostly consist of line segments, which are prominent features in artificial environments. Computing closed-form or approximate affinity fields have deep roots in early vision research [14]. Here, we take a learning-based approach. To enforce the predicted label map to possess certain local structural properties, we propose an affinity field matching loss, which minimizes the discrepancies between the local affinity fields of predictions and ground truth. Additionally, since each category has its own optimal affinity field size, we incorporate *adversarial learning* into affinity field matching to enable adaptive handling. Specifically, we formulate it as a *minimax* problem where we simultaneously maximize the affinity errors from multiple ranges and minimize the overall matching loss. The adversarial network learns to assign smaller affinity fields to “person” than “cow”. Learning by matching adaptive affinity fields has several appealing properties compared to previous works.

1. Our adaptive affinity fields (AAF) naturally encode structural information into segmentation models, equipping them with the “geometric common sense” that is lacking in existing methods.
2. Unlike the popular CRF, our approach introduces no extra parameters during inference. Structural reasoning can be achieved much more efficiently.
3. Instead of modeling appearance-conditioned structures (e.g., RGB values), we operate on the local affinity fields, which characterize the intrinsic geometric regularities inside a given scene. Our approach is more robust to input appearance changes.

Extensive evaluations on the Cityscapes [15] and PASCAL VOC 2012 [16] datasets demonstrate the effectiveness and efficiency of AAF. Our approach also shows much better generalization performance when adapting to the GTA5 [17] dataset.

2 Related Work

Semantic Segmentation. The field of semantic segmentation has witnessed much progress in the last few years. Since the introduction of fully convolutional networks [2], both deeper [4,18,19] and wider [20,21,22] network architectures have been proposed and have dramatically boosted the performance on standard benchmarks like PASCAL VOC 2012 [16]. For example, Wu et al. [4] achieved high segmentation accuracy by replacing backbone networks with the powerful ResNet [3], whereas Yu et al. [22] enabled fine-detailed segmentation results using dilated (i.e., enlarged kernel) convolutions. Though these methods yield impressive performance w.r.t. mIoU (mean intersection over union), they fail to capture abundant structure information present in natural scenes, resulting in “unnatural” parsing results as shown in Fig. 1 (c).

Structure Modeling. To enable geometric common sense for segmentation models, people have explored several ways to incorporate structure information [5,9,6,12,23,24]. For example, Chen et al. [11] utilized denseCRF [5] as post-processing to refine the final segmentation results. Zheng et al. [6] and Liu et al. [12] further made the CRF module differentiable within the deep neural network. Besides, low-level cues, such as affinity [25,26] and contour [27,28] have also been leveraged to encode image structures. However, these methods either are sensitive to transient appearance traits or require expensive iterative inference. In this work we provide another perspective to structure modeling using neighborhood projection matching.

3 Our Approach

Before introducing our adversarial affinity fields summarized in Fig. 2, we first briefly revisit the classic pixel-wise cross-entropy loss used in semantic segmentation.

Per-pixel Supervision. Pixel-wise cross-entropy loss is conventionally used in convolutional neural networks for semantic segmentation [2,11]. It penalizes unary predictions and assumes that the relationship of pixels can be learned inherently in the CNN

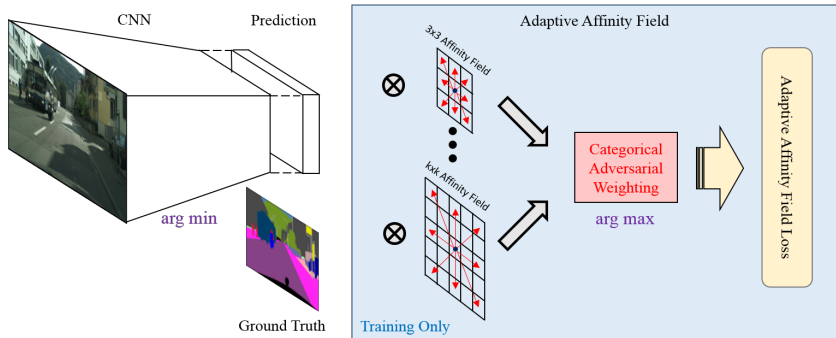


Fig. 2. Architecture for learning semantics segmentation with adaptive affinity fields. The adaptive affinity fields consist of two parts: affinity field projections with multiple kernel sizes and categorical adversarial weighting. Note that the adaptive affinity fields are only imposed during training and introduce no extra computation during inference.

architecture given different sizes of effective receptive fields. The loss is defined as:

$$\mathcal{L}_{\text{unary}} = \frac{1}{n} \sum_{i=1}^n \mathcal{L}_{\text{cross-entropy}}^i = -\log \hat{y}_i(l), \quad (1)$$

where $\hat{y}_i(l)$ is the prediction probability outputted by a segmentation network S at pixel i with the ground truth label l and n is the total number of pixels.

However, this unary loss does not fully incorporate the scene structures. The objects in an image interact with each other in a certain pattern. For example, cars are usually on the road while pedestrians on the sidewalk; buildings are surrounded by the sky but never on top of it; poles are usually vertically straight. Also, some shapes of a certain object occur more frequently, such as rectangles in trains and circles in bikes. This kind of inter-class and inner-class pixel relationships are informative and can be integrated into learning as structure reasoning. We thus propose an additional loss to impose penalties on inconsistent unary predictions and encourage the network to learn intrinsic geometric relationships.

3.1 Pairwise Supervision

Since image structures and object interactions are complicated, it is hard to parameterize them directly with single modularity. Therefore, we decompose those pixel relationships using a certain geometric basis. One projection of a geometric basis captures a certain pixel relationship; the complete set of these projections thus contains rich information of pixel relationships. If two patches of pixel labels are identical, any projection from the two patches should also contain identical structures. Therefore, matching the projections enforces the pixel labels to form desired corresponding relationships.

Projection Matching. The learning by matching projections thus involves designing a set of projection functions and minimizing the distance between the projections of pre-

dictions and ground truth. The projection matching loss is thus formulated as follows:

$$\mathcal{L}_{\text{pairwise}} = \frac{1}{n} \sum_{i=1}^n \mathcal{L}_{\text{projection}}^i = \mathcal{D}(\mathcal{T}(\mathcal{N}(\hat{y}_i)), \mathcal{T}(\mathcal{N}(y_i))), \quad (2)$$

where $\mathcal{D}(\cdot)$ is a certain distance metric, $\mathcal{T}(\cdot)$ is a set of projections, $\mathcal{N}(\cdot)$ denotes the neighborhood, and \hat{y}_i and y_i is the prediction probability and ground truth at pixel i respectively. The unary pixel-wise CNN minimizes the distance between prediction \hat{y}_i and ground truth y_i , while the projection matching loss focuses on the pixel relationships in the neighborhood, or $\mathcal{N}(\hat{y})$ and $\mathcal{N}(y)$. In other words, the projection matching loss encourages CNNs to learn coherent predictions given neighboring pixels.

The objective is thus to minimize the weighted combination of unary and neighborhood losses:

$$S^* = \min_S \mathcal{L} = \min_S \mathcal{L}_{\text{unary}} + \lambda \mathcal{L}_{\text{pairwise}}. \quad (3)$$

Random Projection. One example of projections is the random projection [29]. The random projection reduces dimensionality of input space while retaining a significant degree of the structure. In the context of CNN design, the random basis composes of a number of random convolution filters.

To minimize the distance of the random projections from predictions and ground truth, we adopt the perceptual loss, which is widely used in style transfer and super resolution tasks [30], which has been shown that perceptual losses measure image similarities more robustly than per-pixel losses and thus a strong candidate for measuring random projected features. Therefore, the random projection loss with random projection functions $\phi(\cdot)$ at pixel i can be defined as

$$\mathcal{L}_{\text{random}}^i(\hat{\mathbf{y}}, \mathbf{y}) = \|\phi(\mathcal{N}(\hat{y}_i))\phi(\mathcal{N}(\hat{y}_i))^\top - \phi(\mathcal{N}(y_i))\phi(\mathcal{N}(y_i))^\top\|_F^2. \quad (4)$$

Each random kernel has dimensions of $k \times k \times c_i \times c_o$ where $k \times k$ is the kernel size, c_i corresponds to the number of categories, and c_o is the dimension of output projections. In our experiments, we set kernels as 5×5 and c_o as the same number of c_i . This set of random kernels will enhance both inter- and intra-class interactions with random patterns.

Adversarial Projection. As random projections require a large set of bases and still leave some structures uncovered, learned projections are one step further from random projection. The discriminator D in Generative Adversarial Networks (GANs) [7] can also be viewed as projection matching, which is trained to distinguish real samples from fake samples, which are produced by the generator, or the segmentation network S in this case. The adversarial projection loss can be formulated as

$$\mathcal{L}_{\text{adversarial}}^i = \log D(\mathcal{N}(\hat{y}_i), \mathcal{N}(y_i)) + \log(1 - D(\mathcal{N}(\hat{y}_i))). \quad (5)$$

The distance metric in the adversarial loss is not obvious because it attempts to minimize the instance-to-set distance instead of the usual instance-to-instance distance.

We simultaneously train the segmentation network to minimize $\log(1 - D(\mathcal{N}(\hat{y}_i)))$ and the discriminator to maximize $\log D(\mathcal{N}(\hat{y}_i), \mathcal{N}(y_i))$. In other words, the final objective function for the segmentation network S modeled with a two-player minimax

game is formulated as

$$S^* = \arg \min_S \max_D \mathcal{L}_{\text{unary}} + \mathcal{L}_{\text{adversarial}}. \quad (6)$$

3.2 Affinity Field Projection

The random projections are ineffective due to random kernels and discriminators in GANs are as known hard to train and prone to over-fitting. These drawbacks motivate us to design more flexible and articulated projections: affinity field projection.

Affinity has a long history in computer vision in defining the pixel relationships [31,32]. It considers an image as a graph where a node represents a pixel. The comprehensive graph thus has $n \times n$ edges given n total pixels and can describe an arbitrary relationship between any pair of pixels. To save the complexity while preserving the flexibility, the edges are usually reduced to only connect neighboring pixels given locality. We thus propose affinity field projections to capture flexible pixel relationships. Since the input space is semantic probability space, adding other kernels like Gaussian kernels are unnecessary. Instead, we define the metric of similarity based on Kullback-Leibler divergence, which is also used in the unary metric. Therefore, the affinity field projection loss can be defined as follows:

$$\mathcal{L}_{\text{affinity}}^{ic} = \begin{cases} D_{KL}(\hat{y}_j(c) || \hat{y}_i(c)) & \text{if } y_i(c) = y_j(c) \\ \max\{0, m - D_{KL}(\hat{y}_j(c) || \hat{y}_i(c))\} & \text{otherwise,} \end{cases} \quad (7)$$

where $D_{KL}(\cdot)$ is the Kullback-Leibler divergence defined for two Bernoulli distributions P and Q with parameters p and q respectively: $D_{KL}(P||Q) = p \log \frac{p}{q} + \bar{p} \log \frac{\bar{p}}{\bar{q}}$ for $p, q \in [0, 1]$. For simplicity, we rewrite it as $D_{KL}(p||q)$. If the ground truth label of the pixel i equals to the one of its neighbor j , we minimize the KL divergence; otherwise, we maximize the KL divergence until margin m . The overall loss averages over all categories and pixels.

The projection functions in the affinity field projection are pairwise selection kernels that map a neighborhood into several pairs (8 pairs in our implementation as shown in Fig. 2). The distance metric, however, does not explicitly require the prediction probability to match ground truth. Instead, matching with ground truth projection is modeled through the contour and non-contour terms. The benefit of this formulation is that the predictions are more flexible at the confidence level as long as same-labeled pixels come to a consensus while matching with ground truth would enforce every prediction to be either 0 or 1. For example, if a neighborhood has the affinity pattern of $[0, 1, 1, 0, \dots]$ from ground truth and $[0.05, 0.8, 0.6, 0.01, \dots]$ from predictions, the affinity field loss might push for a solution of $[0.01, 0.7, 0.7, 0.01, \dots]$ where the region of the same object comes to a uniform level of confidence.

The affinity field projection loss encourages two pixels to reach the same prediction probabilities given the same label, i.e., it creates bonds between similar pixels. Given a uniform region, the bonds propagate so that all pixels in the region reach the same status. On the other hand, if two pixels have dissimilar labels, the affinity loss pushes them apart, creating a clear boundary. One of the notorious issue of affinity is the leakage

problem, where pull and push forces meet at open boundaries, i.e., clear boundaries between two regions do not exist. However, we are free to this problem because the affinity field is derived from the ground truth label map and the resulting semantic boundary is always closed. Since the full-ranged affinity field requires unaffordable computations, we model the affinity field within a small neighborhood. In our experiments, 1-affinity field (3×3 kernel size) already demonstrates significant improvements.

The affinity field projections may share some ideas with CRF [5] so as to group or separate pixels. However, a crucial difference is that CRF models require iterative inference to reach a solution while the affinity loss provides direct training guidance on probabilistic semantic predictions. Another similar perspective is the embedding learning with contrastive loss [33], which is commonly used in face identification tasks. The affinity loss works better in segmentation tasks in our experiments because it penalizes the prediction directly and the gradients from KL divergence are aligned with the unary supervision. We include the experimental results in the experiment section.

3.3 Adaptive Kernel Size

Projection matching requires choosing a neighbourhood size, so that pixel-to-pixel relationships can be measured in the same fashion across all locations. However, the ideal size for each category varies with the object size and the boundary shape.

We design a multiscale loss as a weighted sum over different sizes:

$$\mathcal{L}_{\text{multiscale}} = \sum_c \sum_k w_{ck} \mathcal{L}_{\text{pairwise}}^{ck} \quad \text{s.t.} \quad \sum_k w_{ck} = 1 \quad \text{and} \quad w_{ck} \geq 0 \quad (8)$$

where k indicates the kernel size of $k \times k$, and thus $\mathcal{L}_{\text{pairwise}}^{ck}$ and w_{ck} denote the pairwise loss and its weighing w.r.t. kernel size k and category c , respectively.

If we optimize the network together with the loss for w_k , w_k would likely fall into a trivial solution. For example, the affinity loss would be minimum if the smallest kernels are highly weighted for non-contour terms and the largest kernels for contour terms, since nearby pixels are more likely to belong to the same object and far-away pixels to different objects.

To learn the ideal kernel sizes for each category, we instead formulate the solution process as playing a two-player minimax game. That is, the weight for different kernel sizes in the loss should attempt to maximize the total loss in order to penalize critical regions. Our objective for optimizing the network with adaptive kernel sizes thus becomes:

$$S^* = \arg \min_S \max_w \mathcal{L}_{\text{unary}} + \mathcal{L}_{\text{multiscale}}. \quad (9)$$

For the affinity field loss, we can also apply this multiscale loss. We separate the contour term $\mathcal{L}_{\text{affinity}}^{eck}$ and non-contour term $\mathcal{L}_{\text{affinity}}^{\bar{e}ck}$ as their ideal ranges would be different. Finally, we can formulate the adaptive affinity field (AAF) loss as

$$\mathcal{L}_{\text{AAF}} = \sum_c \sum_k (w_{\bar{e}ck} \mathcal{L}_{\text{affinity}}^{\bar{e}ck} + w_{eck} \mathcal{L}_{\text{affinity}}^{eck}). \quad (10)$$

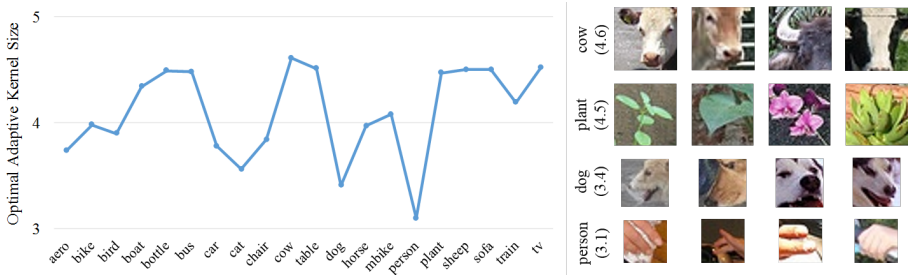


Fig. 3. Left: The optimal kernel size of AAF for each category on PASCAL VOC 2012 validation set. Right: Visualization of image patches with corresponding receptive field size. This visualization depicts how kernel sizes capture the relative sizes in critical regions of different categories.

4 Experiments

We demonstrate the effectiveness of our proposed methods and benchmark our results against state-of-the-art semantic segmentation methods. We first give an overview of the datasets, evaluation metrics, and implementation details used in these experiments.

Dataset. We compare our proposed affinity field and AAF with other competing methods on the PASCAL VOC 2012 [16] and Cityscapes [15] datasets. The Cityscapes dataset focuses on parsing urban street scenes and the VOC dataset is a well-known benchmark for generic image segmentation. We conduct thorough analyses of the proposed methods on VOC dataset and carry out benchmark experiments on both datasets.

Evaluation Metrics. All existing semantic segmentation works employ mean pixel-wise intersection-over-union (denoted as **mIoU**) [2] to evaluate their performance. To fully examine the effectiveness of affinity field projections especially on fine structures, we propose the **instance-wise mIoU** that is computed by normalizing mIoU with number of instances per image, which alleviates the bias toward large objects as in the pixel-wise mIoU. Furthermore, we introduce the de facto standard metrics for boundary detection proposed by [34]. The **boundary detection metrics** compute the correspondences between prediction boundaries and ground truth boundaries, and summarizes the results with precision, recall, and f-measure.

Implementation Details. Our implementation follows the implementation of base architectures, which are PSPNet [18] in most cases or FCN [2]. We use the poly learning rate policy where the current learning rate equals the base one multiplied by $(1 - \frac{\text{iter}}{\text{max_iter}})^{0.9}$. We set the base learning rate as 0.001. The training iterations for all experiments on all datasets are 30K while the performance can be further improved by increasing the iteration number. Momentum and weight decay are set to 0.9 and 0.0005, respectively. For data augmentation, we adopt random mirroring and random resizing between 0.5 and 2 for all datasets. We do not use random rotation and random Gaussian blur. We do not upscale the logits (prediction map) back to the input image resolution,

$k = 3$	$k = 5$	$k = 7$	aero	bike	bird	boat	bottle	bus	car	cat	chair	cow	table	dog	horse	mbike	person	plant	sheep	sofa	train	tv	mIoU
v	x	x	89.02	68.86	90.05	73.52	77.87	94.04	86.94	91.04	40.85	85.82	54.08	84.31	89.12	84.91	86.72	67.52	85.56	52.55	87.60	73.78	79.00
v	v	x	90.19	68.48	89.87	76.91	77.56	93.84	89.08	91.45	40.67	85.82	57.23	85.33	89.77	85.97	86.93	65.68	85.12	52.22	87.25	74.07	79.45
v	v	v	89.45	68.46	90.44	75.82	77.03	94.09	88.01	91.42	38.67	85.98	56.16	84.32	89.22	84.98	87.09	67.35	87.15	55.20	88.22	73.30	79.40

Table 1. Per-category IOU results of AAF with different combinations of kernel sizes k on PASCAL VOC 2012 validation set.

instead, we follow [11]’s setting by downsampling the ground-truth labels for training ($output_stride = 8$).

As is explored in PSPNet [18], larger “cropsizes” and “batchsize” can yield better performance. In the original implementation, “cropsizes” can be up to 720×720 and “batchsize” to 16 using 16 GPUs. To speed up the experiments for validation, we downsize “cropsizes” to 336×336 and “batchsize” to 8 so that a single GTX Titan X GPU is sufficient for training. We set “cropsizes” to 480×480 during inference. We use 4-GPUs to train the network for testing set, which are described in corresponding section.

For random and GAN projections, λ is set to 0.01 for all experiments. For affinity field and AAF projections, λ is set to 0.6 and 1.0 for Cityscapes and VOC, respectively; margin m is set to 3.0 for all experiments. We base our implementations on ResNet101 [3], and we fine-tune models pre-trained on ImageNet [35] for both architectures on VOC and FCN [2] on Cityscapes. For PSPNet [18] implementations on Cityscapes, we fine-tune trained models provided by the authors.

4.1 Analysis

We conduct experiments to analyze the proposed affinity projections. The analyses include 1) effective affinity field size for each category, and 2) effective combinations of affinity field sizes for AAF.

Optimal Adaptive Affinity Field Range. We conduct experiments on PASCAL VOC 2012 with our proposed AAF on three $k \times k$ kernel sizes where $k = 3, 5, 7$. We report the optimal adaptive kernel size on the contour term calculated as $k_c^e = \sum_k w_{eck} \times k$, and summarized in Fig. 3. As shown, “person” and “dog” benefit from smaller kernel size (3.1 and 3.4), while “cow” and “plant” from larger kernel size (4.6 and 4.5). We also display some patches with corresponding receptive field size on the prediction map.

Ablation Study on Combinations of Affinity Field Sizes. We explore the effectiveness of different selections of $k \times k$ kernels, where $k \in \{3, 5, 7\}$, for AAF. Summarized in Table 1, we observe that combinations of 3×3 and 5×5 kernels has the optimal performance, which is roughly equivalent to the additional usage of 7×7 kernel.

4.2 Benchmark

We benchmark our proposed methods on two datasets, PASCAL VOC 2012 [16] and Cityscapes [15]. We include some visual examples to demonstrate the effectiveness of our proposed methods in Fig. 4 and 5.

Method	aero	bike	bird	boat	bottle	bus	car	cat	chair	cow	table	dog	horse	mbike	person	plant	sheep	sofa	train	tv	mIoU
FCN [2]	86.95	59.25	85.18	70.33	73.92	78.86	82.30	85.64	33.57	69.34	27.41	78.04	71.45	70.45	85.54	57.42	71.55	32.48	74.91	59.10	68.91
PSPNet [18]	92.56	66.70	91.10	76.52	80.88	94.43	88.49	93.14	38.87	89.33	62.77	86.44	89.72	88.36	87.48	56.95	91.77	46.23	88.59	77.14	80.12
Affinity	88.66	59.25	87.85	72.19	76.36	80.65	80.74	87.82	35.38	73.45	30.17	79.84	68.15	73.52	87.96	53.95	75.46	37.15	76.62	73.42	71.07
AAF	88.15	67.83	87.06	72.05	76.45	85.43	80.58	88.33	35.47	72.76	31.55	79.68	67.01	77.96	88.20	50.31	73.16	42.71	78.14	73.87	71.95
Random	92.48	67.44	91.99	76.72	77.36	94.92	88.78	91.68	43.70	89.32	62.81	86.61	90.66	87.81	87.20	65.59	88.98	52.22	85.98	75.27	80.61
GAN [8]	92.36	65.94	91.80	76.35	77.70	95.39	89.21	93.30	43.35	89.25	61.81	86.93	91.28	87.43	87.21	68.15	90.64	49.64	88.79	73.83	80.74
Emb.	91.28	69.50	92.62	77.60	78.74	95.03	89.57	93.67	43.21	88.76	62.47	86.68	91.28	88.47	87.44	69.21	91.53	52.17	89.30	74.60	81.36
Affinity	91.52	74.74	92.09	78.17	80.73	95.70	89.52	92.83	43.29	89.21	60.33	87.50	90.96	88.77	88.88	71.00	88.54	50.61	89.64	78.22	81.80
AAF	92.97	73.68	92.49	80.51	79.73	96.15	90.92	93.42	45.11	89.00	62.87	87.97	91.32	90.28	89.30	69.05	88.92	52.81	89.05	78.91	82.39

Table 2. Per-class results on Pascal VOC 2012 validation set.

Method	aero	bike	bird	boat	bottle	bus	car	cat	chair	cow	table	dog	horse	mbike	person	plant	sheep	sofa	train	tv	instance mIoU
PSPNet [18]	87.54	53.08	83.53	76.95	45.13	87.68	68.77	89.01	39.26	88.78	51.49	88.88	84.41	85.95	77.60	48.68	86.25	54.18	88.25	66.11	73.60
Affinity	89.42	61.72	84.64	79.86	57.57	88.81	71.74	88.91	44.78	89.55	52.55	91.22	86.12	87.40	81.10	58.33	85.15	60.61	88.47	68.86	76.73
AAF	89.76	61.74	84.40	81.87	58.04	89.03	73.68	90.46	46.67	89.65	55.63	91.33	85.85	88.36	81.93	59.84	84.52	62.67	89.35	68.80	77.54

Table 3. Per-class instance-wise IoU results on Pascal VOC 2012 validation set.

PASCAL VOC 2012. PASCAL VOC 2012 [16] segmentation dataset contains 20 object categories and one background class. Following the procedure of [2], [18], [11], we use augmented data with the annotations of [36], resulting in 10,582, 1,449, and 1,456 images for training, validation and testing. For training, we first train on *train_aug* for 30K iterations and then fine-tune on *train_val* for another 30K iterations with base learning rate as 0.0001. We follow the hyper-parameter settings mentioned previously. For inference, we further boost the performance by averaging scores from left-right flipped images and multi-scale inputs ($scales = \{0.5, 0.75, 1, 1.25, 1.5, 1.75\}$).

All methods are evaluated by three metrics: mIoU, instance-wise mIoU and boundary detection recall. We first summarized the mIoU results in Table 2. With PSPNet [18] as the base architecture, the VOC results improves consistently from different projections: random projections, GAN projections, affinity field projections and AAF improve the mean IoU by 0.49%, 0.62%, 1.68% and 2.27%. We also compare our proposed affinity field and AAF with embedding projections on VOC. The embedding projection are implemented by imposing contrastive loss [33] on the feature map, which in our implementation is the last convolutional layer before the classifier. We show that affinity-based projections still outperform embedding projections. With FCN [2] as base architecture, affinity field projections and AAF improve the performance by 2.16% and 3.04%. It is worth noting that large improvements over PSPNet are mostly in categories with fine structures, such as “bike”, “chair”, “person”, and “plant”.

Since the pixel-wise mIoU metric is often biased toward large objects, we introduce the instance-wise mIoU to alleviate the bias, which allow us to evaluate fairly the performance on smaller objects. The per category instance-wise mIoU is formulated as $\hat{U}_c = \frac{\sum_x n_{c,x} \times U_{c,x}}{\sum_x n_{c,x}}$, where $n_{c,x}$ and $U_{c,x}$ are the number of instances and IoU of class c in image x , respectively. We report the results in Table 3. In instance-wise mIoU, our AAF is higher than base architecture by 3.94%. As expected, the improvements on categories with smaller sizes are more prominent. For example, the “bottle” is improved by 12.89%.

Next, we analyze quantitatively the improvements of boundary localization. We compute semantic boundaries using pixel-wise semantic predictions and benchmark the results using the standard benchmark for contour detection proposed by [34]. We

Method	aero	bike	bird	boat	bottle	bus	car	cat	chair	cow	table	dog	horse	mbike	person	plant	sheep	sofa	train	tv	mean recall
PSPNet [18]	.694	.420	.658	.417	.624	.626	.562	.667	.297	.587	.279	.667	.608	.513	.554	.235	.547	.413	.551	.512	.527
Affinity	.745	.573	.708	.524	.693	.678	.627	.690	.455	.620	.383	.732	.655	.602	.648	.370	.583	.546	.609	.635	.610
AAF	.746	.559	.704	.524	.684	.675	.622	.701	.441	.612	.391	.728	.653	.595	.647	.355	.580	.547	.608	.628	.606

Table 4. Per-class boundary recall results on Pascal VOC 2012 validation set.

Method	aero	bike	bird	boat	bottle	bus	car	cat	chair	cow	table	dog	horse	mbike	person	plant	sheep	sofa	train	tv	mIoU
PSPNet [18]	94.01	68.08	88.80	64.87	75.87	95.60	89.59	93.15	37.96	88.20	72.58	89.96	93.30	87.52	86.65	61.90	87.05	60.81	87.13	74.65	80.63
AAF	91.25	72.90	90.69	68.22	77.73	95.55	90.70	94.66	40.90	89.53	72.63	91.64	94.07	88.33	88.84	67.26	92.88	62.62	85.22	74.02	82.17

Table 5. Per-class results on Pascal VOC 2012 testing set.

include the boundary recall in Table 4. We omit the precision table due to smaller performance difference. The overall boundary recall is improved by 7.9%. It is worth noting that the boundary recall is improved for every category. This result demonstrates that boundaries of all categories can all benefit from affinity fields and AAF. Among all, the improvements on categories with complicated boundaries, such as “bike”, “bird”, “boat”, “chair”, “person”, and “plant” are significant.

Besides benchmarks, we visualize some examples from the PASCAL VOC validation set for visual quality comparisons in Fig. 4. It is worth noting the prominent visual improvements of the thin structures, that is, the wheels of the bikes and motorcycles and tails of the animals.

Testing Results of VOC 2012. To demonstrate the effectiveness of our method, we test our methods against PSPNet on the test set, and report the mIoU results in Table 5. The training procedure for PSPNet and AAF is the same as follows: We first train the networks on *train_aug* and then fine-tune on *train_val*. Here, we set the “batchsize” to 16 and set “cropsize” to 480×480 for training using 4 GPUs. Our re-trained PSPnet does not reach the same performance as originally reported in the paper because we do not bootstrap the performance by fine-tuning on hard examples (like “bike” images), as pointed out in [37]. We also use left-right flipped images and multi-scale inputs to boost the performance. We demonstrate that our proposed AAF achieve 82.17% mIoU, which is better than re-trained PSPNet by 1.54% and competitive to the state-of-the-art performance.

Cityscapes. Cityscapes [15] is a dataset for semantic urban street scene understanding. It contains 5,000 high quality pixel-level finely annotated images collected from 50

Method	road	swalk	build.	wall	fence	pole	tlight	tsgn	veg.	terrain	sky	person	rider	car	truck	bus	train	mbike	bike	mIoU
FCN [2]	97.31	79.28	89.52	38.08	48.63	49.70	59.37	69.94	90.86	56.58	92.38	75.91	46.24	92.26	50.41	64.51	39.73	54.91	73.07	66.77
PSPNet [18]	98.14	85.02	92.23	49.76	61.44	59.74	69.13	78.39	92.09	62.61	94.19	80.98	59.04	94.81	70.59	82.48	57.22	61.02	76.99	75.05
Affinity	97.52	80.90	90.42	40.45	49.81	55.97	63.92	73.37	91.49	59.01	93.30	78.17	52.16	92.85	52.53	65.78	39.28	52.88	74.53	68.65
AAF	97.58	81.19	90.50	42.30	50.34	57.47	65.39	74.83	91.54	59.25	93.11	78.65	52.98	93.15	53.10	67.58	38.40	51.57	74.80	69.14
CRF [5]	98.13	84.98	92.01	49.90	61.67	55.34	66.96	77.23	91.81	62.76	93.96	80.53	58.58	94.69	70.06	82.45	57.39	60.73	76.56	74.51
GAN [8]	98.09	85.15	92.07	50.74	60.46	59.42	69.27	77.95	92.14	62.08	93.72	80.76	59.27	94.77	73.11	85.96	69.95	65.27	77.22	76.18
Random	98.17	85.06	92.13	52.20	60.04	59.58	69.47	78.52	92.14	61.40	93.70	80.72	58.71	94.77	74.45	84.87	72.31	65.91	77.03	76.39
Affinity	97.99	84.83	92.37	53.86	61.98	61.90	70.67	78.83	92.49	63.40	94.42	81.99	63.36	94.99	79.92	83.49	70.55	65.00	77.24	77.33
AAF	98.04	84.55	92.56	55.04	61.43	62.28	70.51	78.91	92.44	63.40	94.43	81.93	63.14	94.97	79.06	84.10	75.89	65.96	77.49	77.69

Table 6. Per-class results on Cityscapes validation set. Gray colored background denotes using FCN as the base architecture.

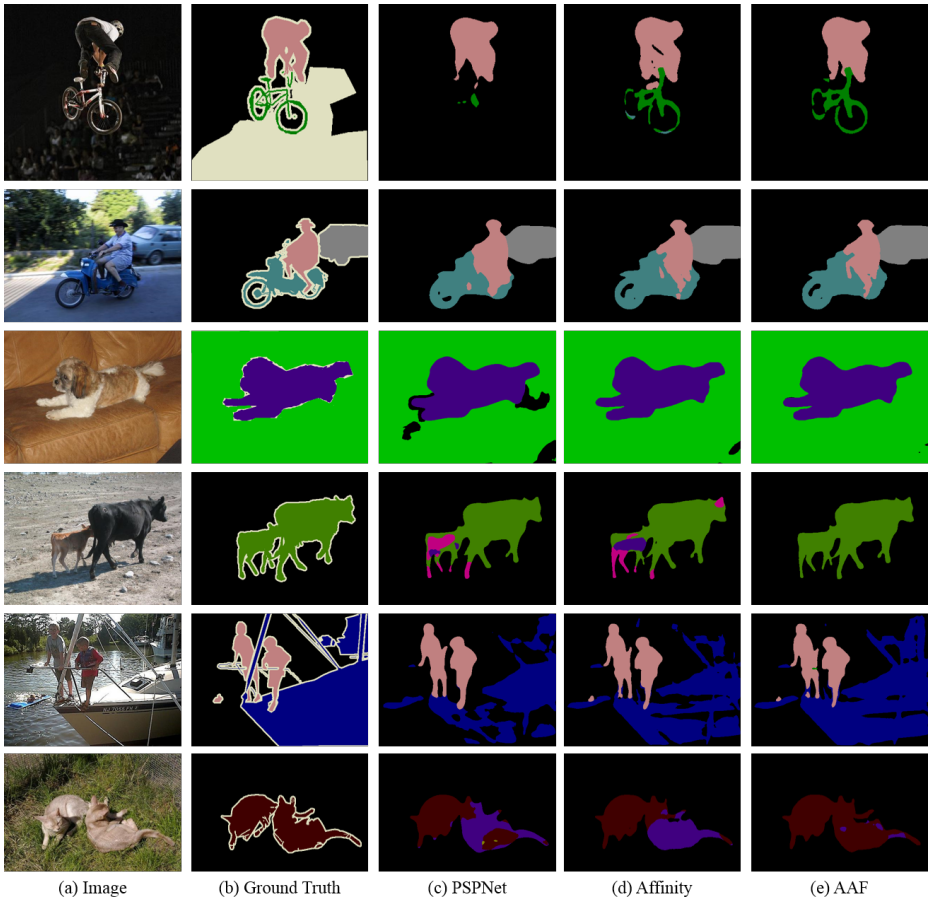


Fig. 4. Visual quality comparisons on the PASCAL VOC 2012 validation dataset: (a) image (b) ground truth (c) PSPNet [18] (d) affinity (e) adaptive affinity fields.

cities in different seasons. The images are divided into training, validation, and testing sets with 2,975, 500, and 1525 images, respectively. It defines 19 categories containing flat, human, vehicle, construction, object, nature, etc.

We do not use multi-scale inputs and left-right flipped images during inference on Cityscapes. Experimental results evaluated using mIoU are summarized in Table 6. Our proposed methods also outperform base architectures consistently: random projections, GAN projections, affinity projections and AAF improve the performance by 1.34%, 1.13%, 2.28% and 2.64%.

As in VOC 2012, we also measure the instance-wise mIoU as summarized in Table 7. Our methods are better than base architecture among most categories. It is worth noting that AAF performs much better than baseline on “mbike” by 36.55%. Likewise, we report boundary recall in Table 8, both affinity field projections and AAF projec-

Method	road	swalk	build.	wall	fence	pole	tlight	tsign	veg.	terrain	sky	person	rider	car	truck	bus	train	mbike	bike	mIoU
PSPNet [18]	97.83	79.11	88.58	36.98	46.31	53.33	52.80	69.46	89.44	41.33	87.58	77.92	77.96	92.32	87.18	93.36	71.30	41.15	72.64	71.40
Affinity	97.70	79.14	88.90	40.66	47.28	55.84	55.48	70.64	89.72	42.26	87.82	78.81	79.27	92.60	87.37	93.85	73.77	71.77	73.60	74.03
AAF	97.72	79.21	88.95	41.49	47.03	56.57	55.97	71.18	89.88	42.64	87.97	78.93	77.51	92.45	87.52	93.83	76.23	77.70	73.76	74.55

Table 7. Per-class instance-wise IOU results on Cityscapes validation set.

Method	road	swalk	build.	wall	fence	pole	tlight	tsign	veg.	terrain	sky	person	rider	car	truck	bus	train	mbike	bike	mean
PSPNet	.475	.813	.635	.497	.613	.656	.705	.753	.693	.630	.620	.780	.683	.832	.637	.773	.564	.602	.747	.669
Affinity	.488	.834	.693	.561	.658	.736	.766	.789	.753	.686	.664	.831	.743	.853	.656	.791	.621	.646	.800	.714
AAF	.490	.843	.718	.576	.669	.766	.783	.806	.775	.698	.681	.846	.758	.858	.662	.796	.639	.655	.823	.728

Table 8. Per-class boundary recall results on Cityscapes validation set.

tions outperform base architecture among all categories. As noted, objects with thin structures are improved most, such as “pole”, “flight”, “person”, “rider”, and “bike”.

Comparison Against CRF. We also report the results of CRF [5] on Cityscapes validation set in Table 6. As is shown, our proposed affinity field and AAF outperform CRF consistently. It is worth mentioning that CRF, as a post-processing method, takes additional 40 seconds to generate the final results on Cityscapes, while our proposed methods have no overhead.

Besides benchmarks, we visualize some examples in Fig. 5 (top 5 rows) from the Cityscapes validation set for visual quality comparison. The visual differences in poles and traffic signs are prominent.

4.3 Generalizability

We further investigate the robustness of our proposed methods on different domains. We train the networks on the Cityscapes dataset [15] and test them on another dataset, Grand Theft Auto V (GTA5) [17] as shown in Fig. 5. The GTA5 dataset is generated from the photo-realistic computer game—*Grand Theft Auto V* [17], which consists of 24,966 images with densely labelled segmentation maps compatible with Cityscapes. We test on GTA5 Part 1, which contains 2,500 images. We summarize the performance in Table 9. It is shown that without fine-tuning, our proposed affinity field projection outperforms the PSPNet [18] baseline model by 9.5% in mean pixel accuracy and 1.46% in mIoU. The results demonstrate the robustness of our proposed methods against appearance variations. Besides benchmarks, we also select some examples from GTA5 for visual quality comparison shown in Fig. 5 (bottom 3 rows).

5 Conclusion

In this work, we propose the adaptive affinity fields for semantic segmentation, which incorporate geometric regularities into segmentation models and learning adaptive kernel sizes with adversarial training. Compared to other alternatives, our adaptive affinity field model is 1) effective (encoding various neighborhood configurations), 2) efficient (introducing no extra parameters), and 3) robust (not sensitive to input appearance changes). Our approach achieves competitive performance on standard benchmarks and also shows great generalization ability on unseen data. We believe it provides a novel perspective towards structure modeling in deep learning.

Method	road	swalk	build.	wall	fence	pole	tlight	tsign	veg.	terrain	sky	person	rider	car	truck	bus	train	mbike	bike	mIoU	pix. acc
PSPNet [18]	61.79	34.26	37.30	13.31	18.52	26.51	31.64	17.51	55.00	8.57	82.47	42.73	49.78	69.25	34.31	18.21	25.00	33.14	6.86	35.06	68.78
Affinity	75.26	30.34	44.10	12.91	20.19	29.78	31.50	23.98	64.25	11.83	74.32	48.28	49.12	67.39	25.76	23.82	20.29	41.48	5.63	36.86	75.13
AAF	83.07	27.82	51.16	10.41	18.76	28.58	31.74	24.98	61.38	12.25	70.65	50.53	48.06	53.35	26.80	20.97	24.50	39.56	9.37	36.52	78.28

Table 9. Per-class results on GTA5 Part 1.

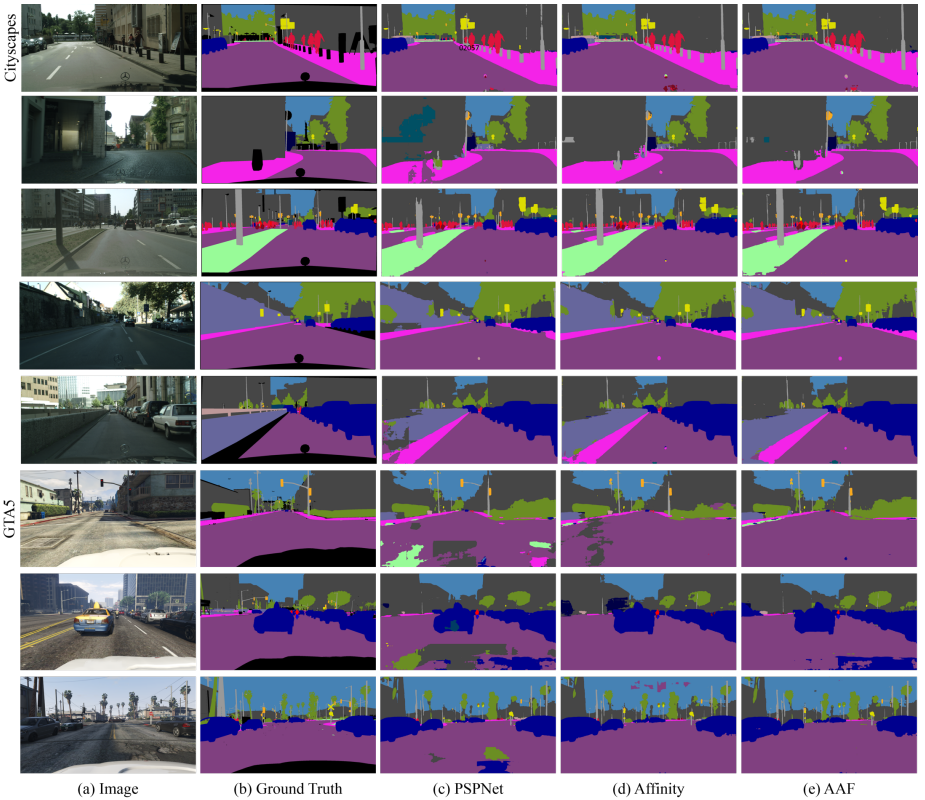


Fig. 5. Top 5 rows: Visual quality comparisons on the Cityscapes [15] validation set: (a) image (b) ground truth (c) PSPNet [18] (d) affinity field projection (e) AAF projection. Bottom 3 rows: The same comparisons on GTA5 [17] part 1.

References

1. Simonyan, K., Zisserman, A.: Very deep convolutional networks for large-scale image recognition. arXiv preprint arXiv:1409.1556 (2014)
2. Long, J., Shelhamer, E., Darrell, T.: Fully convolutional networks for semantic segmentation. In: CVPR. (2015)
3. He, K., Zhang, X., Ren, S., Sun, J.: Deep residual learning for image recognition. In: CVPR. (2016)
4. Wu, Z., Shen, C., Hengel, A.v.d.: High-performance semantic segmentation using very deep fully convolutional networks. arXiv preprint arXiv:1604.04339 (2016)
5. Krähenbühl, P., Koltun, V.: Efficient inference in fully connected crfs with gaussian edge potentials. In: NIPS. (2011)
6. Zheng, S., Jayasumana, S., Romera-Paredes, B., Vineet, V., Su, Z., Du, D., Huang, C., Torr, P.H.: Conditional random fields as recurrent neural networks. In: ICCV. (2015)
7. Goodfellow, I., Pouget-Abadie, J., Mirza, M., Xu, B., Warde-Farley, D., Ozair, S., Courville, A., Bengio, Y.: Generative adversarial nets. In: NIPS. (2014)
8. Luc, P., Couprie, C., Chintala, S., Verbeek, J.: Semantic segmentation using adversarial networks. NIPS Workshop (2016)
9. Chen, L.C., Schwing, A., Yuille, A., Urtasun, R.: Learning deep structured models. In: ICML. (2015)
10. Liu, Z., Li, X., Luo, P., Loy, C.C., Tang, X.: Deep learning markov random field for semantic segmentation. TPAMI (2017)
11. Chen, L.C., Papandreou, G., Kokkinos, I., Murphy, K., Yuille, A.L.: Deeplab: Semantic image segmentation with deep convolutional nets, atrous convolution, and fully connected crfs. arXiv preprint arXiv:1606.00915 (2016)
12. Liu, Z., Li, X., Luo, P., Loy, C.C., Tang, X.: Semantic image segmentation via deep parsing network. In: CVPR. (2015)
13. Radford, A., Metz, L., Chintala, S.: Unsupervised representation learning with deep convolutional generative adversarial networks. arXiv preprint arXiv:1511.06434 (2015)
14. Poggio, T.: Early vision: From computational structure to algorithms and parallel hardware. *Computer Vision, Graphics, and Image Processing* **31**(2) (1985) 139–155
15. Cordts, M., Omran, M., Ramos, S., Rehfeld, T., Enzweiler, M., Benenson, R., Franke, U., Roth, S., Schiele, B.: The cityscapes dataset for semantic urban scene understanding. In: CVPR. (2016)
16. Everingham, M., Van Gool, L., Williams, C.K., Winn, J., Zisserman, A.: The pascal visual object classes (voc) challenge. *IJCV* (2010)
17. Richter, S.R., Vineet, V., Roth, S., Koltun, V.: Playing for data: Ground truth from computer games. In: European Conference on Computer Vision (ECCV). (2016)
18. Zhao, H., Shi, J., Qi, X., Wang, X., Jia, J.: Pyramid scene parsing network. In: CVPR. (2017)
19. Li, X., Liu, Z., Luo, P., Loy, C.C., Tang, X.: Not all pixels are equal: Difficulty-aware semantic segmentation via deep layer cascade. In: CVPR. (2017)
20. Noh, H., Hong, S., Han, B.: Learning deconvolution network for semantic segmentation. In: CVPR. (2015)
21. Ronneberger, O., Fischer, P., Brox, T.: U-net: Convolutional networks for biomedical image segmentation. In: MICCAI. (2015)
22. Yu, F., Koltun, V.: Multi-scale context aggregation by dilated convolutions. In: ICLR. (2016)
23. Lin, G., Shen, C., van den Hengel, A., Reid, I.: Efficient piecewise training of deep structured models for semantic segmentation. In: CVPR. (2016)
24. Bertasius, G., Torresani, L., Yu, S.X., Shi, J.: Convolutional random walk networks for semantic image segmentation. In: CVPR. (2017)

25. Maire, M., Narihira, T., Yu, S.X.: Affinity cnn: Learning pixel-centric pairwise relations for figure/ground embedding. In: CVPR. (2016)
26. Liu, S., De Mello, S., Gu, J., Zhong, G., Yang, M.H., Kautz, J.: Learning affinity via spatial propagation networks. In: NIPS. (2017)
27. Bertasius, G., Shi, J., Torresani, L.: Semantic segmentation with boundary neural fields. In: CVPR. (2016)
28. Chen, L.C., Barron, J.T., Papandreou, G., Murphy, K., Yuille, A.L.: Semantic image segmentation with task-specific edge detection using cnns and a discriminatively trained domain transform. In: CVPR. (2016)
29. Blum, A.: Random projection, margins, kernels, and feature-selection. LNCS (2006)
30. Johnson, J., Alahi, A., Fei-Fei, L.: Perceptual losses for real-time style transfer and super-resolution. In: ECCV. (2016)
31. Shi, J., Malik, J.: Normalized cuts and image segmentation. TPAMI (2000)
32. Yu, S.X., Shi, J.: Multiclass spectral clustering. In: ICCV. (2003)
33. Chopra, S., Hadsell, R., LeCun, Y.: Learning a similarity metric discriminatively, with application to face verification. In: CVPR. (2005)
34. Arbelaez, P., Maire, M., Fowlkes, C., Malik, J.: Contour detection and hierarchical image segmentation. TPAMI (2011)
35. Russakovsky, O., Deng, J., Su, H., Krause, J., Satheesh, S., Ma, S., Huang, Z., Karpathy, A., Khosla, A., Bernstein, M., Berg, A.C., Fei-Fei, L.: Imagenet large scale visual recognition challenge. In: IJCV. (2015)
36. Hariharan, B., Arbeláez, P., Bourdev, L., Maji, S., Malik, J.: Semantic contours from inverse detectors. In: ICCV. (2011)
37. Chen, L.C., Papandreou, G., Schroff, F., Adam, H.: Rethinking atrous convolution for semantic image segmentation. arXiv preprint arXiv:1706.05587 (2017)

6 Appendix

6.1 Additional Experiments on Cityscapes Validation and Test Set

In the paper, we report the mIoU results on Cityscapes [15] validation set with PSP-Net [18] as our base architecture. For our implementations, we fine-tune the trained model provided by the authors. However, fine-tuning from trained models might cause some unwanted problems. Thus, we conduct experiments on Cityscapes by training models from ResNet101 [3] pre-trained on ImageNet [35]. We set the “crop-size” to 720×720 , “batch-size” to 8, train for $90K$ iterations using 4 Titan-X GPUs. For AAF, we set m to 3.0, and use 3×3 and 5×5 kernels. For inference, we set “crop-size” to 720×720 and “stride” to 480×480 .

First we report mIoU on Cityscapes validation set. As shown in Table 10, AAF consistently improves the performance across all classes and is 2.48%. It is worth noting that AAF captures thin-structure classes much better than base architecture, i.e., 5.60% boost in “pole”. Also, large objects are classified more consistently, e.g., 7.30% improvements in “truck” thanks to correct classification of windshields. Additionally, we further boost the performance by using left-right flipped images and multi-scale inputs, which are also shown in Table 10.

Then we evaluate our models on Cityscapes test set, which is shown in Table 11. AAF consistently improves the performance across all classes and is 2.40% higher than base architecture by mIoU. The per-category improvements present the same trend as in the validation set, i.e., 6.22% boost in “pole”.

Method	road	swalk	build.	wall	fence	pole	tlight	tsign	veg.	terrain	sky	person	rider	car	truck	bus	train	mbike	bike	mIoU
PSPNet [18]	97.66	82.13	91.49	51.88	56.89	56.28	65.74	75.02	91.68	62.10	93.99	80.03	60.98	94.35	70.08	83.62	67.93	66.55	76.35	74.99
AAF	97.84	83.54	92.01	55.71	58.30	61.88	70.64	78.46	92.30	63.77	94.40	82.31	64.78	94.92	77.38	86.41	69.11	69.44	78.72	77.47
PSPNet [18]-aug	97.96	83.89	92.22	57.24	59.31	58.89	68.39	77.07	92.18	63.71	94.42	81.80	63.11	94.85	73.54	84.82	67.42	69.34	77.42	76.72
AAF-aug	98.18	85.35	92.86	58.87	61.48	66.64	74.00	80.98	92.95	65.31	94.91	84.27	66.98	95.51	79.39	87.06	67.80	72.91	80.19	79.24

Table 10. Per-class results on Cityscapes validation set. **aug** denotes using left-right flipped images and multi-scale inputs to boost the performance.

Method	road	swalk	build.	wall	fence	pole	tlight	tsign	veg.	terrain	sky	person	rider	car	truck	bus	train	mbike	bike	mIoU
PSPNet [18]	98.16	82.86	91.62	47.04	53.43	55.30	66.52	72.30	92.36	69.88	94.72	82.75	64.20	94.85	68.15	79.60	69.45	63.19	72.07	74.66
AAF	98.32	83.89	92.26	50.31	56.67	61.52	71.78	76.01	93.19	71.11	95.15	84.78	67.75	95.39	70.33	81.51	73.56	66.15	74.40	77.06

Table 11. Per-class results on Cityscapes test set.